Heisenberg-limited Sagnac interferometer with multiparticle states

Chengyi Luo,[1,2] Jiahao Huang,[1,*] Xiangdong Zhang,[1,2] and Chaohong Lee[1,3,†]

[1]*TianQin Research Center & School of Physics and Astronomy, Sun Yat-Sen University (Zhuhai Campus), Zhuhai 519082, China*

[2]*School of Physics, Sun Yat-Sen University (Guangzhou Campus), Guangzhou 510275, China*

[3]*State Key Laboratory of Optoelectronic Materials and Technologies, Sun Yat-Sen University (Guangzhou Campus), Guangzhou 510275, China*

(Received 1 November 2016; revised manuscript received 29 December 2016; published 10 February 2017)

The Sagnac interferometry has widely been used to measure rotation frequency. Beyond the conventional single-particle scheme, we propose a multiparticle scheme via Bose condensed atoms. In our scheme, an ensemble of entangled two-state Bose atoms are moved in a ring via a state-dependent rotating potential, and then the atoms are recombined for interference via Ramsey pulses. The phase accumulation time is determined by the state-dependent rotating potential. The ultimate rotation sensitivity can be improved to the Heisenberg limit if the initial internal degrees of freedom are entangled. By implementing parity measurement, the ultimate measurement precision can be saturated, and the achieved measurement precisions approach the Heisenberg limit. Our results provide a promising way to exploit many-body quantum entanglement in precision rotation sensing.

DOI: 10.1103/PhysRevA.95.023608

I. INTRODUCTION

Various advantages of quantum metrology [1–7] have been demonstrated by neutral atoms [8–10], trapped ions [11], and photons [12], etc. Generally speaking, the measurement precision $\Delta\chi$ via N-independent particles is imposed by the standard quantum limit (SQL): $\Delta\chi \propto 1/\sqrt{N}$ [13]. However, by utilizing multiparticle entanglement and squeezing, the SQL can be surpassed [13–19]. The Greenberger-Horne-Zeilinger (GHZ) state [20] and the NOON state [21] can improve the minimum uncertainty to the so-called Heisenberg limit [13,16,17]: $\Delta\chi \propto 1/N$. It has also been demonstrated that the achievable precision can beat the SQL or even approach the Heisenberg limit by using spin squeezed states [1,2,4,5], twin Fock states [3], and spin cat states [22]. Up to now, quantum metrology has extensively been used in high-precision sensing of rotations [23–25], accelerations [26], magnetic fields [4,5], gravitational fields [27,28], etc.

Rotation sensing is essential in both fundamental sciences and practical technologies from determining the Earth's rotation frequency to building gyroscopes for navigation [29]. The Sagnac effect describes the phase-shift accumulation between two counterpropagating waves around a closed path in a rotating frame [30]. Based upon the Sagnac effect, Sagnac interferometers for measuring rotation frequency have been realized via ring lasers [31], atoms [32–35], and trapped ions [36]. Recently, a Sagnac interferometry with a single-atom clock [37] have been proposed via combing the techniques of state-dependent manipulations and Ramsey pulses.

Beyond the single-particle scheme, it is interesting to investigate how to exploit many-body quantum entanglement in a precision measurement of rotation frequency. On one hand, due to their robust quantum coherence and high controllability, several entangled states of ultracold atoms (in particular Bose condensed atoms) have been generated in experiments [1,2,4,5]. On the other hand, ring traps and state-dependent manipulation of Bose condensed atoms [38–43] have been demonstrated. Combing these techniques, it is possible to realize the Sagnac interferometer with multiparticle entangled states of Bose condensed atoms. Unlike other conventional interferometers, the external and internal degrees of freedom couple with each other during the phase accumulation in our Sagnac interferometry. Thus, the measurement precision of rotation frequency is affected sensitively by both the estimated angular frequency itself and the induced angular frequency. To achieve the best sensitivity, it is important to optimally control the angular frequency.

This article is organized as follows. In Sec. II, we introduce the single-particle Sagnac interferometry scheme and present our multiparticle Sagnac interferometry scheme with entangled Bose condensed atoms. In Sec. III, we calculate the ultimate rotation measurement precision and find the measurement precision may reach the Heisenberg limit. The uncertainty of the estimated angular frequency ω_s depends on the induced angular frequency ω_p as well as the rotation frequency ω_s to be measured. We also derive an analytic quantum Cramer-Rao bound (QCRB) for some specific choices of ω_p and ω_s. In Sec. IV, we further investigate the rotation frequency estimation via parity measurement. We find that parity measurement is an optimal and realizable way to obtain the Heisenberg-limited precision. Meanwhile, we also derive an analytic formula for the uncertainty of rotation frequency via parity measurement. In Sec. V, we mainly discuss the experimental possibility of our scheme, including the effects of imperfect state preparation. In Sec. VI, we briefly summarize and outlook our scheme.

II. SAGNAC INTERFEROMETRY VIA STATE-DEPENDENT MANIPULATION

In this section, as the basis of our multiparticle scheme, we first introduce the scheme of a Sagnac interferometer with

*hjiahao@mail2.sysu.edu.cn; eqjiahao@gmail.com

†lichaoh2@mail.sysu.edu.cn; chleecn@gmail.com

a single particle [37]. Then, we describe our multiparticle Sagnac interferometry scheme with Bose condensed atoms by using the input maximally entangled state.

A. Single-particle scheme

The Sagnac interferometer with a single particle combines the state-dependent potentials moving around a ring with a sequence of Ramsey pulses [37]. The interferometry involves two atomic internal states $|\uparrow\rangle$ and $|\downarrow\rangle$. For a one-dimensional model, the atom is assumed to be tightly confined within a ring with fixed radius r, and the motional degrees of freedom are restricted to the azimuthal angle θ. Initially, the atom is prepared in an internal state $\frac{1}{\sqrt{2}}(|\uparrow\rangle + |\downarrow\rangle)$ by a $\pi/2$ pulse at the location $\theta = 0$. The two components are guided in opposite directions along the circular paths due to the state-dependent rotating potentials. When the two components recombine, they will acquire a relative phase, which can be extracted by applying a second $\pi/2$ pulse and measuring the final population difference.

The spin-dependent manipulation with a single two-level atom is characterized by the Hamiltonian,

$$\hat{H}_{\text{single}}(t) = \hat{H}_{\uparrow}(t)|\uparrow\rangle\langle\uparrow| + \hat{H}_{\downarrow}(t)|\downarrow\rangle\langle\downarrow|. \tag{1}$$

In the inertial frame, the explicit expressions for $\hat{H}_{\uparrow}(t)$ and $\hat{H}_{\downarrow}(t)$ are

$$\begin{aligned}\hat{H}_{\sigma}(t) &= \hbar\omega\hat{a}^{\dagger}\hat{a} + i\sqrt{\frac{m\hbar\omega}{2}}r(\hat{a}^{\dagger} - \hat{a})[\omega_s + \eta_{\sigma}\omega_p(t)] \\ &= \hat{H}_0 + \hat{H}^I_{\sigma}(t),\end{aligned} \tag{2}$$

where $\sigma = \uparrow, \downarrow$ and ω is the trapping frequency of the harmonic potential along the radial direction. $\hat{a}^{\dagger}$ and $\hat{a}$ are the creation and annihilation operators acting on the external state of the atom. The symbols $\eta_{\uparrow} = +1$ and $\eta_{\downarrow} = -1$ account for the opposite rotational directions for the two spin components.

When the Hamiltonian (1) is time dependent, it does not commute with itself at different times, i.e., $[\hat{H}(t), \hat{H}(t')] \neq 0$. Thus, one cannot evaluate the evolution operator by mere integration. To solve this problem, one can use the Magnus expansion [44]. Suppose that the evolution operator of the system can be expressed as

$$\hat{U}_{\sigma}(t) = \hat{U}_0(t)\hat{U}^I_{\sigma}(t), \tag{3}$$

with

$$\hat{U}_0(t) = \exp\left(-i\frac{\hat{H}_0}{\hbar}t\right). \tag{4}$$

Substitute Eqs. (3) and (4) into the Schrödinger equation, and one can find out that the operator $\hat{U}^I_{\sigma}(t)$ satisfies

$$\begin{aligned}\frac{\partial\hat{U}^I_{\sigma}(t)}{\partial t} &= \left[\hat{U}^{\dagger}_0(t)\frac{-i\hat{H}^I_{\sigma}}{\hbar}\hat{U}_0(t)\right]\hat{U}^I_{\sigma}(t) \\ &= \xi_{\sigma}(t)(e^{-i\omega t}\hat{a} - e^{i\omega t}\hat{a}^{\dagger}),\end{aligned} \tag{5}$$

with

$$\xi_{\sigma}(t) = \sqrt{\frac{m\omega}{2\hbar}}r[\omega_s + \eta_{\sigma}\omega_p(t)]. \tag{6}$$

Applying the Magnus expansion, one can obtain

$$\hat{U}^I_{\sigma}(T) = \exp(\alpha^*_{\sigma}\hat{a} - \alpha_{\sigma}\hat{a}^{\dagger})\exp(i\phi_{\sigma}), \tag{7}$$

where

$$\alpha_{\sigma} = \int_0^T \xi_{\sigma}(t)e^{i\omega t}dt, \tag{8}$$

and

$$\phi_{\sigma} = \int_0^T\int_0^{t_1} \xi_{\sigma}(t_1)\xi_{\sigma}(t_2)\sin[\omega(t_1 - t_2)]dt_2dt_1. \tag{9}$$

Here, T is the total evolution time, and T is determined by the choice of $\omega_p(t)$ satisfying $\int_0^T \omega_p(t)dt = \pi$. Therefore, the final form of the evolution operator reads

$$\hat{U}_{\sigma} = \exp(-i\omega t\hat{a}^{\dagger}\hat{a})\exp(\alpha^*_{\sigma}\hat{a} - \alpha_{\sigma}\hat{a}^{\dagger})\exp(i\phi_{\sigma}). \tag{10}$$

The above expressions are general results for time-dependent parameter $\omega_p(t)$ and are valid for fixed parameter ω_p as well.

B. Multiparticle scheme

Inspired by the above single-particle scheme, we propose to implement multiparticle entangled states for Sagnac interferometry. We aim to investigate how to utilize the multiparticle entangled states to improve the measurement precision of the Sagnac interferometry. In our scheme, by using Bose condensed atoms, the multiparticle Sagnac interferometry also consists of state-dependent potentials and a sequence of Ramsey pulses. The two atomic hyperfine states ($|m_F = 1\rangle \equiv |\uparrow\rangle$ and $|m_F = -1\rangle \equiv |\downarrow\rangle$) label the two evolution paths. Each atom may occupy one of the two hyperfine states and can be regarded as a spin-$\frac{1}{2}$ particle with $\hat{\sigma}_z|\uparrow\rangle = +|\uparrow\rangle$ and $\hat{\sigma}_z|\downarrow\rangle = -|\downarrow\rangle$. Initially, all atoms locate at $\theta = 0$, and their external states are prepared in the ground-state $|0\rangle$ of the harmonic potential along the radial direction.

The multiatom Sagnac interferometry includes the following steps. First, a desired multiparticle state is prepared as the input state. For our input state, only the spin degrees of freedom are entangled, whereas the external degrees of freedom are identical in $|0\rangle$. Then, the spin-dependent trapping potentials for $|\uparrow\rangle$ and $|\downarrow\rangle$ rotate along opposite directions with angular frequencies $+\omega_p(t)$ and $-\omega_p(t)$, respectively. During the free evolution, an ω_s-dependent phase-shift $\phi(\omega_s)$ between two counterpropagating modes is accumulated. Finally, the two modes encounter on the other side, and a $\pi/2$ pulse is applied for recombination. The unknown angular frequency ω_s is extracted by measuring the population information of the spin states. The schematic of our multiparticle Sagnac interferometry is shown in Fig. 1. s

The biggest difference between multiparticle and single-particle schemes is embodied in the input states. The input entangled states can improve the rotation sensitivity. Here, we consider the maximally entangled state (the GHZ state) as the

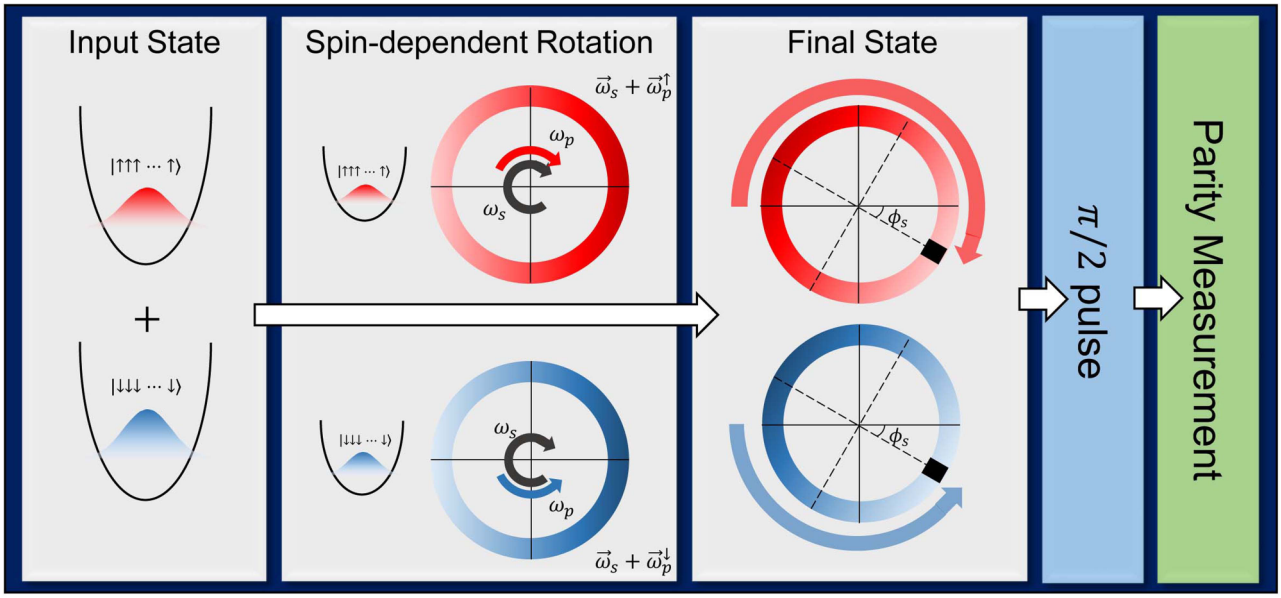

FIG. 1. Schematic of the multiatom Sagnac interferometry. Initially, the system is prepared in the internal GHZ state between two hyperfine levels ($|m_F = 1\rangle$ and $|m_F = -1\rangle$). Then, a state-dependent evolution is applied for accumulating a relative phase dependent on the rotation angular frequency ω_s. Finally, after a $\pi/2$ pulse for the two hyperfine states, the parity measurement is used to extract the relative phase, and the rotation angular frequency ω_s is derived from the relative phase.

input state. The input GHZ state is written as

$$|\Psi\rangle_{\rm in}^{\rm GHZ} = \frac{1}{\sqrt{2}}\left[\bigotimes_{k=1}^{N}(|\uparrow\rangle|0\rangle)_k + \bigotimes_{k=1}^{N}(|\downarrow\rangle|0\rangle)_k\right], \tag{11}$$

where the internal states of each particle are maximally entangled. By using the nonlinear effects due to atom-atom interaction, the GHZ state can be prepared via dynamical evolution [45,46] or ground-state preparation [46–48]. The preparation of the GHZ state will be discussed in Sec. VI.

After input state preparation, the system will undergo a dynamical evolution to accumulate a phase shift between the two spin components. The two different spin components rotate in opposite directions with angular velocity $\omega_p(t)$ around the ring trapping potentials, which can be described by the Hamiltonian,

$$\hat{H}(t) = \sum_{k=1}^{N}\hat{H}_k(t), \hat{H}_k(t) = \hat{H}_\uparrow(t)|\uparrow\rangle\langle\uparrow| + \hat{H}_\downarrow(t)|\downarrow\rangle\langle\downarrow|. \tag{12}$$

where $\hat{H}_k$ is the single-atom Hamiltonian for the kth particle. Since the single-atom Hamiltonians for different atoms and different components commute with each other, i.e., $[\hat{H}_l(t), \hat{H}_k(t)] = 0 (l \neq k)$ and $[\hat{H}_\uparrow(t), \hat{H}_\downarrow(t)] = 0$, the evolution operator for total evolution time T can be formally written as

$$\hat{U}(T) = \prod_{k=1}^{N}\hat{U}_k(T), \quad \hat{U}_k(T) = \hat{U}_\uparrow(T)|\uparrow\rangle\langle\uparrow| + \hat{U}_\downarrow(T)|\downarrow\rangle\langle\downarrow|, \tag{13}$$

with $\hat{U}(T)$ and $\hat{U}_k(T)$ being the evolution operators of the system and the individual atom, respectively. Also, T is the total evolution time, and T is determined by the choice of $\omega_p(t)$ satisfying $\int_0^T \omega_p(t)dt = \pi$.

Similar to the single-particle scheme, the multiparticle state-dependent evolution operator (13) can be derived by following the procedures of Eqs. (3)–(10). The evolution operator characterizes the dynamics of the counterrotation for the two spin components. It indicates that the effect of the rotation is equivalent to the displacement operator, the phase accumulation with eigenfrequency, and the state-dependent phase shift. By applying the evolution operator (13) on the initial state, the output state after the free evolution becomes

$$\begin{aligned}|\Psi(\omega_s)\rangle_{\rm out} &= \hat{U}(T)|\Psi\rangle_{\rm in} \\ &= \frac{1}{\sqrt{2}}\left[\bigotimes_{k=1}^{N}[\hat{U}_\uparrow(T)|\uparrow\rangle|0\rangle]_k + \bigotimes_{k=1}^{N}[\hat{U}_\downarrow(T)|\downarrow\rangle|0\rangle]_k\right].\end{aligned} \tag{14}$$

Here, the information of the parameter ω_s is imprinted in the output state of the system $|\Psi(\omega_s)\rangle_{\rm out}$. Finally, we can acquire the value of ω_s from measuring the output state $|\Psi(\omega_s)\rangle_{\rm out}$ and estimate the uncertainty of the parameter $\Delta\omega_s$.

At first, we vary both ω_s and ω_p in a wide range continuously and calculate the corresponding output states. Interestingly, we found that the external part of the output state is sensitively affected by the choice of ω_s and ω_p. For the kth particle, the different choices of ω_s and ω_p lead to different fidelities between the evolved external state $|\psi_{\rm ex}\rangle_k$ and its initial ground-state $F_0 = |_k\langle\psi_{\rm ex}|0\rangle_k|^2$. The fidelity F_0 can characterize the probability of the atoms staying in the initial ground state of the external potential. In Fig. 2(d), we plot the phase diagram of the fidelity F_0 with $\omega_s, \omega_p \in [0, \omega]$. For most ω_s's, the dark regions ($F_0 \ll 1$) alternate with the bright regions ($F_0 \approx 1$) as ω_p increases from 0 to ω. F_0

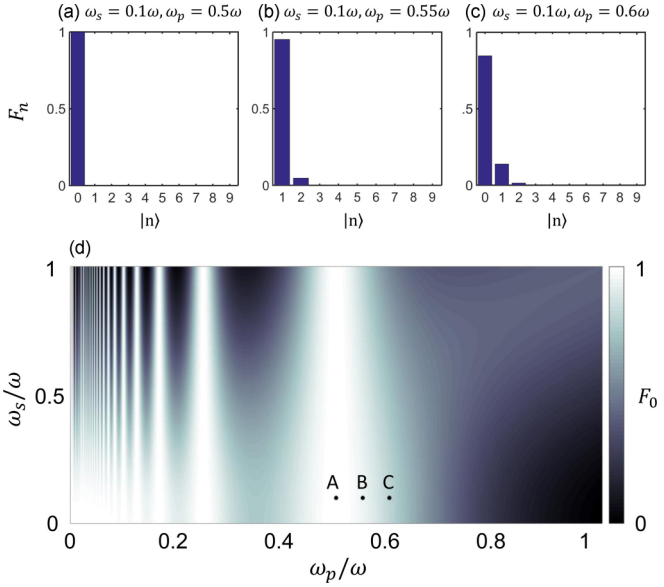

FIG. 2. The phase diagram of fidelity between its evolved external state and the initial ground-state $F_0 = |_k\langle\psi_{\rm ex}|0\rangle_k|^2$. The distributions of fidelity $F_n = |_k\langle\psi_{\rm ex}|n\rangle_k|^2$ for (a) $\omega_s = 0.1\omega$, $\omega_p = 0.5\omega$, (b) $\omega_s = 0.1\omega$, $\omega_p = 0.55\omega$, and (c) $\omega_s = 0.1\omega$, $\omega_p = 0.6\omega$ are shown. Here $|0\rangle$ is the external ground state of the potential well, and $|n\rangle$ is the nth excited state ($n \geqslant 1$). The numerical results are obtained with $\omega = 1$.

oscillates rapidly when ω_p is relatively small, and a large bright area appears in the center of $\omega_p = 0.5\omega$. In the brightest line where $F_0 = 1$ (e.g., $\omega_p = 0.5\omega$), the external state of every atom stays in the ground state all the time, and the system's external state can be assumed to be unchanged during the Sagnac phase accumulation. In general, it is beneficial to keep the external state unchanged during the interferometry and exploit the entanglement among the internal states of the atoms to perform high-precision measurement.

Obviously, the largest bright area is in the vicinity of $\omega_p/\omega = 0.5$. We fix $\omega_s = 0.1\omega$ and choose $\omega_p = 0.5\omega, 0.55\omega, 0.6\omega$ to illustrate the distribution of fidelities projecting on $|n\rangle$, where $|0\rangle$ is the external ground state and $|n\rangle$ is the nth external excited state ($n \geqslant 1$), see Figs. 2(a)–2(c). For $\omega_p = 0.5\omega$, the external state stays in $|0\rangle$. Whereas for $\omega_p = 0.55\omega$ and $\omega_p = 0.6\omega$, F_0 decreases, and the evolved external state has some components of other excited states $|n\rangle$. It is shown that one can specifically choose $\omega_p = 0.5\omega$ to measure the rotation frequency ω_s since the fidelity F_0 is very close to 1 in the vicinity of $\omega_p = 0.5\omega$. This can tolerate a small deviation of ω_p/ω around 0.5 if some unavoidable errors exist.

Based on the phase diagram of Fig. 2(d), one can carefully vary ω_p according to ω_s to ensure that $F_0 \simeq 1$. Under this situation, the external state can be truncated only at the ground state. In the following, we will show that this situation is advantageous for the high-precision Sagnac interferometry and the Heisenberg-limited measurement can be achieved. In addition, by using this truncation, some analytic results can be derived, see Secs. IV and V.

III. ULTIMATE ANGULAR FREQUENCY MEASUREMENT PRECISION

In the framework of the quantum metrology, for a parameter-dependent output state, the uncertainty of the estimated parameter is limited by the QCRB,

$$\Delta\omega_s \geqslant \Delta\omega_s^Q \equiv \frac{1}{\sqrt{\nu F_Q(\omega_s)}}, \tag{15}$$

where ν is the times of independent experiments and the uncertainty is defined as $\Delta\omega_s = \sqrt{\langle\omega_s^2\rangle - \langle\omega_s\rangle^2}$. $F_Q(\omega_s)$ is the so-called quantum Fisher information (QFI), which can be expressed as a function of the output state $|\Psi(\omega_s)\rangle_{\rm out}$ and its derivative with respect to the parameter ω_s, i.e.,

$$F_Q(\omega_s) = 4[\langle\Psi'(\omega_s)|\Psi'(\omega_s)\rangle - |\langle\Psi'(\omega_s)|\Psi(\omega_s)\rangle_{\rm out}|^2], \tag{16}$$

with $|\Psi'(\omega_s)\rangle = d|\Psi(\omega_s)\rangle_{\rm out}/d\omega_s$. The QFI determines the ultimate value of a parameter uncertainty for a given parameter-dependent output state. The larger QFI $F_Q(\omega_s)$ corresponds to a smaller parameter uncertainty $\Delta\omega_s$.

In turns of our protocol, we first choose some specific values of ω_s and ω_p which satisfies $F_0 \approx 1$ according to Fig. 2(d). In this case, the external state can be truncated only at the ground-state $|0\rangle$. Thereafter, the explicit expressions of $\Delta\omega_s^Q$ and the QFI $F_Q(\omega_s)$ could be evaluated. The output state can be calculated as

$$\begin{aligned}|\Psi(\omega_s)\rangle_{\rm out} &\approx \frac{1}{\sqrt{2}}\bigotimes_{k=1}^{N}[e^{-(|\alpha_\uparrow|^2/2)}e^{i\phi_\uparrow}|0\rangle|\uparrow\rangle]_k \\ &\quad + \frac{1}{\sqrt{2}}\bigotimes_{k=1}^{N}[e^{-(|\alpha_\downarrow|^2/2)}e^{i\phi_\downarrow}|0\rangle|\downarrow\rangle]_k \\ &= \frac{1}{\sqrt{2}}\left[C_\uparrow^N\bigotimes_{k=1}^{N}|\uparrow\rangle_k|0\rangle_k + C_\downarrow^N\bigotimes_{k=1}^{N}|\downarrow\rangle_k|0\rangle_k\right].\end{aligned} \tag{17}$$

Here, the coefficients $C_\uparrow$ and $C_\downarrow$, respectively, are

$$C_\uparrow = e^{(mr^2/2\hbar\omega)(\omega_s+\omega_p)^2\mathscr{X}}e^{i(mr^2/2\hbar\omega)(\omega_s+\omega_p)^2\mathscr{Y}}, \tag{18}$$

and

$$C_\downarrow = e^{(mr^2/2\hbar\omega)(\omega_s-\omega_p)^2\mathscr{X}}e^{i(mr^2/2\hbar\omega)(\omega_s-\omega_p)^2\mathscr{Y}}, \tag{19}$$

with

$$\mathscr{X} = 1 - \cos\left(\frac{\pi\omega}{\omega_p}\right), \quad \mathscr{Y} = \frac{\pi\omega}{\omega_p} - \sin\left(\frac{\pi\omega}{\omega_p}\right). \tag{20}$$

Then, its derivative with respect to ω_s is as follows:

$$\begin{aligned}|\Psi'(\omega_s)\rangle &= \frac{d|\Psi(\omega_s)\rangle_{\rm out}}{d\omega_s} \\ &= \frac{1}{\sqrt{2}}\left[NC_\uparrow^{N-1}C_\uparrow'\bigotimes_{k=1}^{N}|\uparrow\rangle_k|0\rangle_k\right. \\ &\quad \left. + NC_\downarrow^{N-1}C_\downarrow'\bigotimes_{k=1}^{N}|\downarrow\rangle_k|0\rangle_k\right].\end{aligned} \tag{21}$$

Thus, we could calculate the QFI through Eq. (16), and its final expression can be written as

$$F_Q(\omega_s) = \frac{m^2N^2A^2}{\hbar^2\omega^2\omega_p^2\pi^2}\left(2\omega_p^2\mathscr{X} + 2\pi\omega\omega_p\mathscr{Y} - \pi^2\omega^2\right) \times\{2D_-^N(\omega_p-\omega_s)^2 + 2D_+^N(\omega_p+\omega_s)^2 - [D_-^N(\omega_s-\omega_p) + D_+^N(\omega_s+\omega_p)]^2\}. \quad (22)$$

In which $A = \pi r^2$ is the area of the enclosed ring and

$$D_+ = \exp\left[-\frac{mr^2(\omega_s+\omega_p)^2\mathscr{X}}{\hbar\omega}\right],$$
$$D_- = \exp\left[-\frac{mr^2(\omega_s-\omega_p)^2\mathscr{X}}{\hbar\omega}\right]. \quad (23)$$

According to Eq. (22), specifically when $\omega_p = \omega/2L$ [$L = 1,2,3,\ldots$, which correspond to the brightest vertical lines in Fig. 2(d)], $\mathscr{X} = 0$, and $\mathscr{Y} = \pi\omega/\omega_p$, the expression of Eq. (22) can be simplified. Surprisingly, the QFI is exactly proportional to the square of the total particle number, i.e.,

$$F_Q(\omega_s) = \frac{4N^2m^2A^2}{\hbar^2} = \left(\frac{2NmA}{\hbar}\right)^2. \quad (24)$$

Therefore, the ultimate measurement precision with the GHZ state can be derived

$$\Delta\omega_s^{\mathrm{GHZ}} \propto \frac{1}{\sqrt{F_Q(\omega_s)}} = \frac{\hbar}{2mA}\frac{1}{N}. \quad (25)$$

The uncertainty $\Delta\omega_s^{\mathrm{GHZ}}$ is inversely proportional to the total atomic number N with a prefactor $\hbar/2mA$. The prefactor is the same as the one with single-atom Sagnac interferometry [37]. When inputting an atomic spin coherent state (SCS) $|\Psi\rangle_{\mathrm{in}}^{\mathrm{SCS}} = \bigotimes_{k=1}^N [\frac{1}{\sqrt{2}}(|\uparrow\rangle + |\downarrow\rangle)|0\rangle]_k$ (N-independent atoms in the same state), the ultimate measurement precision of ω_s is just bounded by the SQL, i.e., $\Delta\omega_s^{\mathrm{SCS}} = \hbar/(2mA\sqrt{N})$. It is shown that, compared with the single-particle scheme, the measurement precision of ω_s in Sagnac interferometry can be improved to the Heisenberg limit by using the input GHZ state.

Furthermore, to verify the above analytic results, we follow the standard procedure and calculate the QFI numerically. For $\omega_s = 0.1\omega$ and $\omega_p = 0.5\omega$, the numerical calculation agrees with the analytic result perfectly. It confirms the validity of the truncation at the external ground state under this situation. On the other hand, we choose other parameters that do not meet the condition of $F_0 \approx 1$. For $\omega_s = 0.1\omega$, $\omega_p = 0.55\omega$ and $\omega_s = 0.1\omega$, $\omega_p = 0.6\omega$, the QFIs also exhibit quadratic dependence on the total particle number. The quadratic dependence is insensitive to the choices of ω_s and ω_p. In order to show the relation clearly, we give the log-log scaling of $F_Q(\omega_s)$ with respect to N under the above three sets of ω_s and ω_p, see Fig. 3. The slopes of the three lines are all nearly 2, which confirm that $F_Q(\omega_s) \propto N^2$.

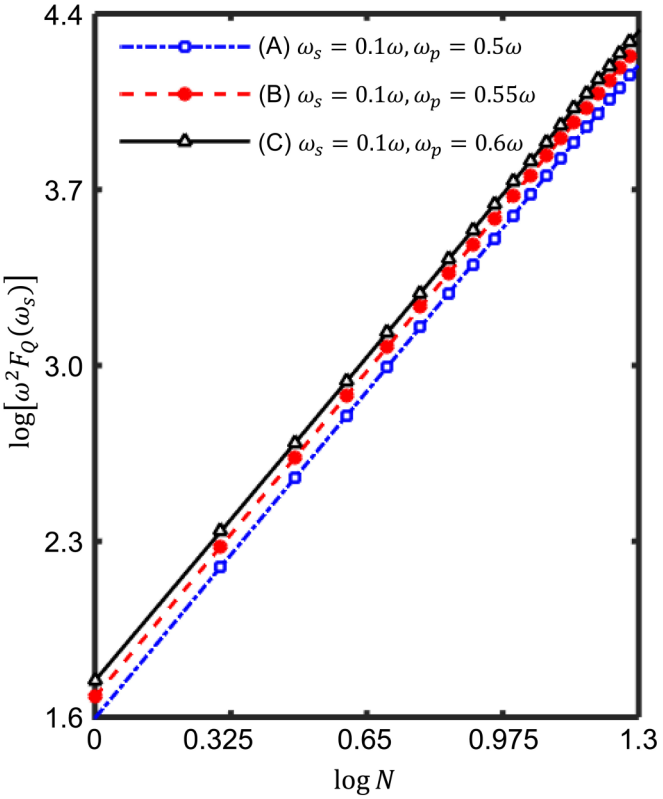

FIG. 3. The log-log scaling of QFI versus the total particle number N under different choices of ω_s and ω_p. The slopes of the lines are approximately equal to 2, which indicate $F_Q(\omega_s) \propto N^2$. To perform the numerical calculation, here we set $\omega = 1$, $\hbar = 1$, $m = 1$, and $r = 1$.

IV. PARITY MEASUREMENT

The ultimate measurement precision obtained via QFI is a theoretical bound which is independent of the choices of observable measurements. In realistic scenarios, one would also be interested in how to approach the QCRB via certain achievable measurements. For the maximally entangled state, parity measurement is assumed to be one of the effective candidates to saturate the QCRB and attain the Heisenberg limit [49–53].

In our scheme, we also try to evaluate the rotation measurement precision via parity measurement. The parity operator for $|\downarrow\rangle$ can be expressed as $\hat{P} = \exp[i\pi(\sum_{k=1}^N |\downarrow\rangle_k\langle\downarrow|_k)] = \exp[i\pi(\frac{N}{2} - \sum_{k=1}^N \hat{\sigma}_z^{(k)})]$. In Sec. II, we have presented the dynamical evolution and the output state (14). Before the parity measurement, a $\pi/2$ pulse is implemented to rotate the output state for recombination, i.e, $|\Psi\rangle_f = \exp(-i\frac{\pi}{2}\hat{R})|\Psi\rangle_{\mathrm{out}}$, where $\hat{R} = \frac{1}{2}\sum_{k=1}^N \hat{\sigma}_y^{(k)}$ with $\hat{\sigma}_y^{(k)} = \frac{1}{2i}(|\downarrow\rangle_k\langle\uparrow|_k - |\uparrow\rangle_k\langle\downarrow|_k)$. The average of the parity measurement for $|\downarrow\rangle$ is written as $\langle\hat{P}\rangle =_f \langle\Psi|\hat{P}|\Psi\rangle_f$, and the corresponding variance is given by $(\Delta\hat{P})^2 = \langle\hat{P}^2\rangle - \langle\hat{P}\rangle^2$. Finally, from the results of the parity measurement, the corresponding uncertainty of parameter ω_s can be estimated. The standard deviation $\Delta\omega_s$ can be evaluated with the error propagation formula,

$$\Delta\omega_s = \frac{\Delta\hat{P}}{|\partial\langle\hat{P}\rangle/\partial\omega_s|}. \quad (26)$$

Still, we first apply the approximation that the external state is restricted in the ground state for the specified range of ω_s

and ω_p according to Fig. 2(d). Following the above procedure with the approximation, the final state after an additional $\pi/2$ pulse would be as follows:

$$
\begin{aligned}
|\Psi\rangle_f &= \exp\left(-i\frac{\pi}{2}\hat{R}\right)\hat{U}|\Psi\rangle_{\text{in}} \\
&\approx \frac{1}{\sqrt{2}}\bigotimes_{k=1}^{N}\left[\left(\frac{|\uparrow\rangle+|\downarrow\rangle}{2}\right)\bigotimes\exp\left(-\frac{|\alpha_\uparrow|^2}{2}\right)\exp(i\phi_\uparrow)|0\rangle\right]_k \\
&\quad+\frac{1}{\sqrt{2}}\bigotimes_{k=1}^{N}\left[\left(\frac{|\downarrow\rangle-|\uparrow\rangle}{2}\right)\bigotimes\exp\left(-\frac{|\alpha_\downarrow|^2}{2}\right)\exp(i\phi_\downarrow)|0\rangle\right]_k. \qquad (27)
\end{aligned}
$$

Applying the parity measurement $\hat{P}$ on the final state, the expectation value of the parity measurement can be obtained

$$
\langle\hat{P}\rangle = {}_f\langle\Psi|\hat{P}|\Psi\rangle_f = \frac{(-1)^N\cos\left(\frac{2N\omega_s mr^2\omega_p}{\hbar\omega}\mathscr{Y}\right)}{e^{(Nmr^2/\hbar\omega)(\omega_p^2+\omega_s^2)\mathscr{X}}}, \qquad (28)
$$

$$
\langle\hat{P}^2\rangle = {}_f\langle\Psi|\hat{P}^2|\Psi\rangle_f = \frac{e^{-(Nmr^2/\hbar\omega)(\omega_p-\omega_s)^2\mathscr{X}}+e^{-(Nmr^2/\hbar\omega)(\omega_p+\omega_s)^2\mathscr{X}}}{2}. \qquad (29)
$$

Meanwhile, the variance of the parity measurement for the final state can also be given by

$$
(\Delta\hat{P})^2 = \frac{e^{-(Nmr^2/\hbar\omega)(\omega_p-\omega_s)^2\mathscr{X}}+e^{-(Nmr^2/\hbar\omega)(\omega_p+\omega_s)^2\mathscr{X}}}{2}-\frac{\cos^2\left(\frac{2N\omega_s mr^2\omega_p}{\hbar\omega}\mathscr{Y}\right)}{e^{(2Nmr^2/\hbar\omega)(\omega_p^2+\omega_s^2)\mathscr{X}}}. \qquad (30)
$$

Eventually, we can obtain the standard deviation of ω_s,

$$
\begin{aligned}
\Delta\omega_s &= \frac{\Delta\hat{P}}{|\partial\langle\hat{P}\rangle/\partial\omega_s|} \\
&= \frac{e^{(Nmr^2/\hbar\omega)(\omega_p^2+\omega_s^2)\mathscr{X}}\sqrt{e^{-(Nmr^2/\hbar\omega)(\omega_p-\omega_s)^2\mathscr{X}}+e^{-(Nmr^2/\hbar\omega)(\omega_p+\omega_s)^2\mathscr{X}}-2e^{-(2Nmr^2/\hbar\omega)(\omega_p^2+\omega_s^2)\mathscr{X}}\cos^2\left(\frac{2Nmr^2\omega_p\omega_s}{\hbar\omega}\mathscr{Y}\right)}}{2\sqrt{2}\frac{Nmr^2}{\hbar\omega}\left|\omega_s\mathscr{X}\cos\left(\frac{2Nmr^2\omega_p\omega_s}{\hbar\omega}\mathscr{Y}\right)+\omega_p\mathscr{Y}\sin\left(\frac{2Nmr^2\omega_p\omega_s}{\hbar\omega}\mathscr{Y}\right)\right|}. \qquad (31)
\end{aligned}
$$

Here, specifically when $\omega_p=\omega/2L$ [$L=1,2,3,\ldots$, which correspond to the brightest vertical lines in Fig. 2(d)], $\mathscr{X}=0$, $\mathscr{Y}=\pi\omega/\omega_p$, Eqs. (28)–(31) could be simplified further to

$$
\langle\hat{P}\rangle = (-1)^N\cos\left(\frac{2NmA\omega_s}{\hbar}\right), \qquad (32)
$$

$$
\langle\hat{P}^2\rangle = 1, \qquad (33)
$$

$$
(\Delta\hat{P})^2 = \sin\left(\frac{2NmA\omega_s}{\hbar}\right), \qquad (34)
$$

and

$$
\Delta\omega_s = \frac{\hbar}{2mA}\frac{1}{N}. \qquad (35)
$$

From Eq. (35), it is clearly shown that the deviation of ω_s is exactly consistent with the ultimate bound Eq. (25) predicted with the QFI.

Meanwhile, we check the above analytic results by numerical calculation. The numerical results via parity measurement for $N=5$ are presented in Figs. 4(a) and 4(b). For $\omega_p=0.5\omega$, the expectation values of parity oscillate sinusoidally from -1 to 1 with respect to ω_s. The deviation $\Delta\omega_s$ is a horizontal line versus ω_s, which is independent of ω_s. This result perfectly agrees with the analytic Eq. (35). On the other hand, we also evaluate $\Delta\omega_s$ via parity measurement with $\omega_p=0.55\omega$ and $\omega_p=0.6\omega$. The contrast of $\langle\hat{P}\rangle$ drops rapidly as ω_p/ω becomes far away from 0.5. The period of the sinusoidal oscillation also changes. These result in the reduction of the measurement precision.

Based on our numerical calculation, we confirm that the best standard deviation of ω_s can be achieved under the choice of $\omega_p=0.5\omega$.

Finally, we fix $\omega_p=0.5\omega$ and evaluate the log-log scaling of $\Delta\omega_s$ versus the total particle number N, see Fig. 4(c). Compared with the input coherent spin state (which is equivalent to the single-particle scheme), the dependence of the deviation $\Delta\omega_s$ on N based upon our scheme is quadratic rather than linear. Thus, by implementing the input GHZ state for Sagnac interferometry, the parity measurement is an optimal way to saturate the ultimate precision bound and can be used to perform high-precision rotation sensing at the Heisenberg limit.

V. EXPERIMENTAL POSSIBILITY

We have shown how many-body entanglement of the GHZ state enhances the rotation sensitivity. The GHZ state can be prepared by various methods [47,54,55]. For Bose condensed atoms, the GHZ state can be created by dynamical nonlinear evolution [45,46] or adiabatic ground-state preparation [46,47]. By driving internal state Raman transitions via

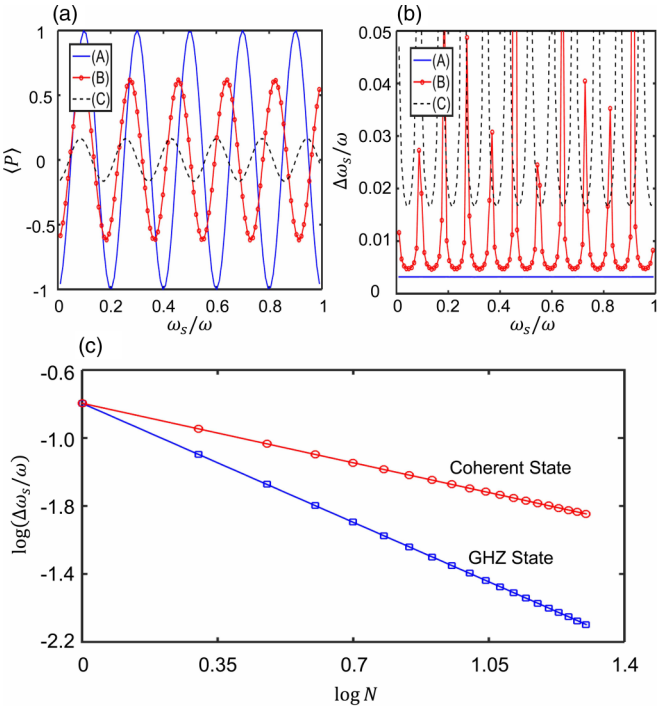

FIG. 4. Numerical results of the parity measurement. (a) The expectation value of the parity is a sinusoidal function with respect to ω_s. (b) The dependence of the measurement precision on ω_s itself. For (a) and (b), (A) $\omega_p = 0.5\omega$, (B) $\omega_p = 0.55\omega$, and (C) $\omega_p = 0.6\omega$, and the total particle number $N = 5$. (c) For case (A), the log-log scaling of QFI versus N with the input GHZ state and spin coherent state are shown, respectively. Here, we set $\omega = 1$, $\hbar = 1$, $m = 1$, and $r = 1$.

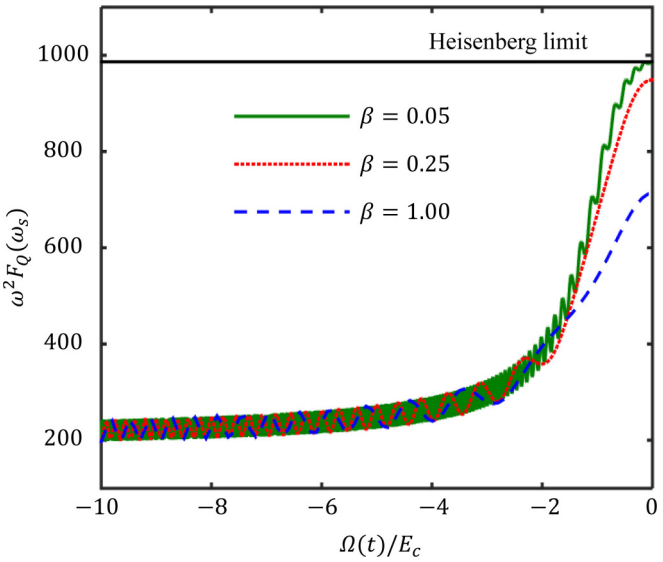

FIG. 5. The influences of nonadiabatic ground-state preparation for the input state. Here, β characterizes the adiabaticity of the sweeping. We set $\omega = 1$, $\hbar = 1$, $m = 1$, $r = 1$, and $\omega_p/\omega = 0.5$ for numerical calculation. The total atomic number is chosen as $N = 5$.

laser pulses [54] or classical fields [55], an N-GHZ state can also be generated effectively in spin-1 Bose-Einstein condensates. In addition, the spin-dependent control is another important element in our scheme, which may be realized by adiabatic dressed potentials. State-dependent control of atomic transport in the toroidal trap has been proposed [41]. The rf dressed potential and the coherent control atomic motion have been demonstrated in experiments [38–40,42,43]. These techniques could be applied to perform the state-dependent control of atomic transport on the ring-shaped traps [56]. On the other hand, our Sagnac interferometry scheme could be applied to other many-body systems, such as trapped ions [11]. A protocol for using trapped ions to measure rotations via repeated round-trip Sagnac interferometry was proposed recently [36]. By using the GHZ state [57], the rotation sensitivity can also be improved.

Finally, we focus on the generation of a GHZ state via ground-state preparation in Bose-Josephson systems. The two-mode Bose-Josephson Hamiltonian reads [1,2,4,46]

$$H_{\mathrm{BJ}} = \Omega \hat{J}_\gamma + \delta \hat{J}_z + \frac{E_c}{2}\hat{J}_z^2, \tag{36}$$

where Ω is the Josephson coupling strength, δ is the asymmetry between the two modes, and E_c corresponds to the atom-atom interaction. $\hat{J}_\gamma = \cos\gamma \hat{J}_x + \sin\gamma \hat{J}_y$ with $\hat{J}_{x,y,z} = \frac{1}{2}\sum_{k=1}^{N} \sigma_{x,y,z}^{(k)}$ as the collective spin operators and γ as an adjustable angle. In this system, the atom-atom interaction can be tuned via some of the techniques, such as Feshbach resonance [1,10]. By using the adiabatic ground-state preparation in symmetric Bose-Josephson systems ($\delta = 0$) with negative nonlinearity ($E_c < 0$), the GHZ state can be generated [47]. Ideally, one can choose E_c as a negative value, prepare the system $H_{\mathrm{BJ}} = \Omega_0 \hat{J}_x + \frac{E_c}{2}\hat{J}_z^2$ in the strong-coupling regime ($\Omega_0/|E_c| \gg 1$), and then linearly decrease Ω to zero [$\Omega(t)/|E_c| = \Omega_0/|E_c| - \beta t$ with $\beta = (\Omega_0/|E_c|)T_s^{-1}$ and T_s as the dimensionless total sweeping time]. If the sweeping is slow enough, $\beta \ll 1$, the system state will evolve along the instant ground state of the Hamiltonian $H_{\mathrm{BJ}}(t) = \Omega(t)\hat{J}_x + \frac{E_c}{2}\hat{J}_z^2$. Thus, when $\Omega(t) = 0$, the system evolves into a GHZ state where the negative E_c ensures the appearance of the dynamical bifurcation [22,47,48].

However, in realistic experiments, the initial state may not be in the ground state, and the sweeping may be nonadiabatic. These may cause the imperfect preparation of the input GHZ state. We consider that the initial state is prepared in a spin coherent state $|\mathrm{SCS}\rangle = \bigotimes_{k=1}^{N} [\frac{1}{\sqrt{2}}(|\uparrow\rangle + |\downarrow\rangle)]_k$, which is more feasible in experiments. Then, we vary the Josephson coupling strength from Ω_0 to zero according to $\Omega(t)/|E_c| = \Omega_0/|E_c| - \beta t$. The system state will evolve under the Hamiltonian $H_{\mathrm{BJ}}(t) = \Omega(t)\hat{J}_x + \frac{E_c}{2}\hat{J}_z^2$. The sweeping rate β characterizes the adiabaticity. Here, we obtain the evolved states during the sweeping with different β's numerically. Based on the evolved states, we calculate the corresponding QFI under the ideal selection of ω_p, see Fig. 5.

Since the initial spin coherent state is not the eigenstate of the Hamiltonian, the QFI oscillates during the sweeping. However, the amplitude of the oscillation is relatively small. When β tends to be adiabatic (e.g., $\beta = 0.05$), the QFI of the prepared state can approach the Heisenberg limit. When the sweeping becomes faster (β increases), the QFI of the prepared state gradually drops. However, for a modest sweeping rate (e.g., $\beta = 0.25$), the QFI of the prepared state is still close to the Heisenberg limit. It is shown that, under the modest

nonadiabatic of sweeping, the ground-state preparation is still effective and the prepared input state may still achieve a high-precision measurement of ω_s near the Heisenberg limit.

VI. SUMMARY AND DISCUSSION

To summarize, we have presented a multiatom Sagnac interferometer scheme with a maximally entangled state, which can attain the Heisenberg limit. During the Sagnac phase accumulation, the internal and external states of the system are coupled with each other. The uncertainty of the estimated angular frequency ω_s is sensitively influenced by the choice of the induced angular frequency ω_p. By optimally selecting ω_p, the external state would stay in its initial ground state during the phase accumulation, and the ultimate angular frequency measurement precision can reach the Heisenberg limit. Furthermore, we analyzed the angular frequency estimation via the parity measurement. We found that the parity measurement may attain the Heisenberg limit imposed by the quantum Fisher information. Finally, we discuss the experimental possibility and the influences of imperfect preparation of the maximally entangled state. Our scheme can also be extended to other kinds of many-body entangled states, such as spin squeezed states [15], spin cat states [22], or the twin Fock state [51]. This may open up a way to perform a high-precision rotation measurement with many-body quantum entanglement beyond the standard single-particle Sagnac effect.

ACKNOWLEDGMENTS

This work was supported by the National Basic Research Program of China (Grant No. 2012CB821305) and the National Natural Science Foundation of China (Grants No. 11374375 and No. 11574405). J.H. was partially supported by the National Postdoctoral Program for Innovative Talents of China (Program No. BX201600198). C.L. would like to thank W. Campbell, S. Zhang, Z. Tao, and J. Chen for helpful discussions.

[1] C. Gross, T. Zibold, E. Nicklas, J. Estève, and M. K. Oberthaler, Nonlinear atom interferometer surpasses classical precision limit, Nature (London) **464**, 1165 (2010).

[2] M. F. Riedel, P. Böhi, Y. Li, T. W. Hänsch, A. Sinatra, and P. Treutlein, Atom-chip-based generation of entanglement for quantum metrology, Nature (London) **464**, 1170 (2010).

[3] B. Lücke, M. Scherer, J. Kruse, L. Pezzé, F. Deuretzbacher, P. Hyllus, O. Topic, J. Peise, W. Ertmer, J. Arlt, L. Santos, A. Smerzi, and C. Klempt, Twin matter waves for interferometry beyond the classical limit, Science **334**, 773 (2011).

[4] C. F. Ockeloen, R. Schmied, M. F. Riedel, and P. Treutlein, Quantum Metrology with A Scanning Probe Atom Interferometer, Phys. Rev. Lett. **111**, 143001 (2013).

[5] W. Muessel, H. Strobel, D. Linnemann, D. B. Hume, and M. K. Oberthaler, Scalable Spin Squeezing for Quantum-Enhanced Magnetometry with Bose-Einstein Condensates, Phys. Rev. Lett. **113**, 103004 (2014).

[6] H. Strobel, W. Muessel, D. Linnemann, T. Zibold, D. B. Hume, L. Pezzè, A. Smerzi, M. K. Oberthaler, Fisher information and entanglement of non-Gaussian spin states, Science **345**, 424 (2014).

[7] G. Vasilakis, H. Shen, K. Jensen, M. Balabas, D. Salart, B. Chen, and E. S. Polzik, Generation of a squeezed state of an oscillator by stroboscopic back-action-evading measurement, Nat. Phys. **11**, 389 (2015).

[8] J. Fortágh and C. Zimmermann, Magnetic microtraps for ultracold atoms, Rev. Mod. Phys. **79**, 235 (2007).

[9] I. Bloch, J. Dalibard, and W. Zwerger, Many-body physics with ultracold gases, Rev. Mod. Phys. **80**, 885 (2008).

[10] C. Chin, R. Grimm, P. Julienne, and E. Tiesinga, Feshbach resonances in ultracold gases, Rev. Mod. Phys. **82**, 1225 (2010).

[11] D. Leibfried, R. Blatt, C. Monroe, and D. Wineland, Quantum dynamics of single trapped ions, Rev. Mod. Phys. **75**, 281 (2003).

[12] J. M. Raimond, M. Brune, and S. Haroche, Manipulating quantum entanglement with atoms and photons in a cavity, Rev. Mod. Phys. **73**, 565 (2001).

[13] V. Giovannetti, S. Lloyd, and L. Maccone, Quantum-enhanced measurements: beating the standard quantum limit, Science **306**, 1330 (2004).

[14] D. J. Wineland, J. J. Bollinger, W. M. Itano, and F. L. Moore, Spin squeezing and reduced quantum noise in spectroscopy, Phys. Rev. A **46**, R6797(R) (1992).

[15] M. Kitagawa and M. Ueda, Squeezed spin states, Phys. Rev. A **47**, 5138 (1993).

[16] V. Giovannetti, S. Lloyd, and L. Maccone, Quantum Metrology, Phys. Rev. Lett. **96**, 010401 (2006).

[17] V. Giovannetti, S. Lloyd, and L. Maccone, Advances in quantum metrology, Nat. Photonics **5**, 222 (2011).

[18] C. Lee, J. Huang, H. Deng, H. Dai, and J. Xu, Nonlinear quantum interferometry with Bose condensed atoms, Front. Phys. **7**, 109 (2012).

[19] J. Huang, S. Wu, H. Zhong, and C. Lee, Quantum Metrology with Cold Atoms, Annu. Rev. Cold At. Mol. **2**, 365 (2014).

[20] D. Leibfried, M. D. Barrett, T. Schaetz, J. Britton, J. Chiaverini, W. M. Itano, J. D. Jost, C. Langer, and D. J. Wineland, Toward Heisenberg-limited spectroscopy with multiparticle entangled states, Science **304**, 1476 (2004).

[21] P. Kok, H. Lee, and J. P. Dowling, Creation of large-photon-number path entanglement conditioned on photodetection, Phys. Rev. A **65**, 052104 (2002).

[22] J. Huang, X. Qin, H. Zhong, Y. Ke, and C. Lee, Quantum metrology with spin cat states under dissipation, Sci. Rep. **5**, 17894 (2015).

[23] S. A. Haine, Mean-Field Dynamics and Fisher Information in Matter Wave Interferometry, Phys. Rev. Lett. **116**, 230404 (2016).

[24] S. P. Nolan, J. Sabbatini, M. W. J. Bromley, M. J. Davis, and S. A. Haine, Quantum enhanced measurement of rotations with a spin-1 Bose-Einstein condensate in a ring trap, Phys. Rev. A **93**, 023616 (2016).

[25] S. Ragole and J. M. Taylor, Interacting Atomic Interferometry for Rotation Sensing Approaching the Heisenberg Limit, Phys. Rev. Lett. **117**, 203002 (2016).

[26] A. Peters, K. Y. Chung, and S. Chu, Measurement of gravitational acceleration by dropping atoms, Nature (London) **400**, 849 (1999).

[27] J. Aasi *et al.* (LIGO Scientific Collaboration), Enhanced sensitivity of the LIGO gravitational wave detector by using squeezed states of light, Nat. Photonics **7**, 613 (2013).

[28] B.P. Abbott *et al.* (LIGO Scientific Collaboration and Virgo Collaboration), Observation of Gravitational Waves from a Binary Black Hole Merger, Phys. Rev. Lett. **116**, 061102 (2016).

[29] T. L. Gustavson, P. Bouyer, and M. A. Kasevich, Precision Rotation Measurements with an Atom Interferometer Gyroscope, Phys. Rev. Lett. **78**, 2046 (1997).

[30] E. J. Post, Sagnac effect, Rev. Mod. Phys. **39**, 475 (1967).

[31] K. U. Schreiber, T. Klügel, J.-P. R. Wells, R. B. Hurst, and A. Gebauer, How to Detect the Chandler and the Annual Wobble of the Earth with a Large Ring Laser Gyroscope, Phys. Rev. Lett. **107**, 173904 (2011).

[32] A. Lenef, T. D. Hammond, E. T. Smith, M. S. Chapman, R. A. Rubenstein, and D. E. Pritchard, Rotation Sensing with an Atom Interferometer, Phys. Rev. Lett. **78**, 760 (1997).

[33] T. L. Gustavson, A. Landragin, and M. A. Kasevich. Rotation sensing with a dual atom-interferometer Sagnac gyroscope, Class. Quantum Grav. **17**, 2385 (2000).

[34] A. Gauguet, B. Canuel, T. Lévèque, W. Chaibi, and A. Landragin, Characterization and limits of a cold-atom Sagnac interferometer, Phys. Rev. A **80**, 063604 (2009).

[35] G. Tackmann, P. Berg, C. Schubert, S. Abend, M. Gilowski, W. Ertmer, and E. M. Rasel, Self-alignment of a compact large-area atomic Sagnac interferometer, New J. Phys. **14**, 015002 (2012).

[36] W. C. Campbell, P. Hamilton, Rotation sensing with trapped ions, arXiv:1609.00659, [J. Phys. B: At. Mol. Opt. Phys. (to be published)].

[37] R. Stevenson, M. R. Hush, T. Bishop, I. Lesanovsky, and T. Fernholz, Sagnac Interferometry with a Single Atomic Clock, Phys. Rev. Lett. **115**, 163001 (2015).

[38] P. Treutlein, P. Hommelhoff, T. Steinmetz, T. W. Hänsch, and J. Reichel, Coherence in Microchip Traps, Phys. Rev. Lett. **92**, 203005 (2004).

[39] T. Schumm, S. Hofferberth, L. M. Andersson, S. Wildermuth, S. Groth, I. Bar-Joseph, J. Schmiedmayer, and P. Krüger, Matter-wave interferometry in a double well on an atom chip, Nat. Phys. **1**, 57 (2005).

[40] O. Morizot, Y. Colombe, V. Lorent, H. Perrin, and B. M. Garraway, Ring trap for ultracold atoms, Phys. Rev. A **74**, 023617 (2006).

[41] T. Fernholz, R. Gerritsma, P. Krüger, and R. J. C. Spreeuw, Dynamically controlled toroidal and ring-shaped magnetic traps, Phys. Rev. A **75**, 063406 (2007).

[42] B. E. Sherlock, M. Gildemeister, E. Owen, E. Nugent, and C. J. Foot, Time-averaged adiabatic ring potential for ultracold atoms, Phys. Rev. A **83**, 043408 (2011).

[43] R. Szmuk, V. Dugrain, W. Maineult, J. Reichel, and P. Rosenbusch, Stability of a trapped-atom clock on a chip, Phys. Rev. A **92**, 012106 (2015).

[44] S. Blanesa, F. Casasb, J. A. Oteoc, and J. Rosc, The Magnus expansion and some of its applications, Phys. Rep. **470**, 151 (2009).

[45] K. Pawlowski, D. Spehner, A. Minguzzi, and G. Ferrini, Macroscopic superpositions in Bose-Josephson junctions: Controlling decoherence due to atom losses, Phys. Rev. A **88**, 013606 (2013).

[46] C. Gross, Spin squeezing, entanglement and quantum metrology with Bose-Einstein condensates, J. Phys. B: At. Mol. Opt. Phys. **45**, 103001 (2012).

[47] C. Lee, Adiabatic Mach-Zehnder Interferometry on a Quantized Bose-Josephson Junction, Phys. Rev. Lett. **97**, 150402 (2006).

[48] C. Lee, Universality and Anomalous Mean-Field Breakdown of Symmetry-Breaking Transitions in a Coupled Two-Component Bose-Einstein Condensate, Phys. Rev. Lett. **102**, 070401 (2009).

[49] J. J. Bollinger, W. M. Itano, D. J. Wineland, and D. J. Heinzen, Optimal frequency measurements with maximally correlated states, Phys. Rev. A **54**, R4649(R) (1996).

[50] C. C. Gerry, and R. A. Campos, Generation of maximally entangled states of a Bose-Einstein condensate and Heisenberg-limited phase resolution, Phys. Rev. A **68**, 025602 (2003).

[51] R. A. Campos, C. C. Gerry, and A. Benmoussa, Optical interferometry at the Heisenberg limit with twin fock states and parity measurements, Phys. Rev. A **68**, 023810 (2003).

[52] C. C. Gerry and J. Mimih, Heisenberg-limited interferometry with pair coherent states and parity measurements, Phys. Rev. A **82**, 013831 (2010).

[53] S. A. Haine and S. S. Szigeti, Usefulness of entanglement-assisted quantum metrology, Phys. Rev. A **92**, 032317 (2015).

[54] L. You, Creating Maximally Entangled Atomic States in a Bose-Einstein Condensate, Phys. Rev. Lett. **90**, 030402 (2003).

[55] M. Zhang and L. You, Quantum Zeno Subspace and Entangled Bose-Einstein Condensates, Phys. Rev. Lett. **91**, 230404 (2003).

[56] T. Fernholz *et al.*, Towards rotation sensing with a single atomic clock, Proc. SPIE, **9900**, 990007 (2016).

[57] T. Monz, P. Schindler, J. T. Barreiro, M. Chwalla, D. Nigg, W. A. Coish, M. Harlander, W. Hänsel, M. Hennrich, and R. Blat, 14-Qubit Entanglement: Creation and Coherence, Phys. Rev. Lett. **106**, 130506 (2011).